Repair of Ni-based single-crystal superalloys using vacuum plasma spray

T. Kalfhaus [a,*], M. Schneider [b], B. Ruttert [b], D. Sebold [a], T. Hammerschmidt [c], J. Frenzel [b], R. Drautz [c], W. Theisen [b], G. Eggeler [b], O. Guillon [a,d], R. Vassen [a]

[a] Forschungszentrum Jülich GmbH, 52425 Jülich, Germany
[b] Ruhr-Universität Bochum, 44801 Bochum, Germany
[c] ICAMS, Ruhr-Universität Bochum, 44801 Bochum, Germany
[d] Jülich Aachen Research Alliance: JARA-Energy, Forschungszentrum Jülich GmbH, 52425 Jülich, Germany

HIGHLIGHTS

- Vacuum plasma spray is used for the deposition of CMSX-4 powder on heated single crystalline CMSX-4 substrates.
- Coatings with different spray parameters were produced to identify the condition for optimum mechanical properties.
- A HIP is used to promote grain growth, decrease the porosity and achieve the desired microstructure.
- The microstructure of the interface region and the coating was characterised in the as-spayed and the HIP condition.

GRAPHICAL ABSTRACT
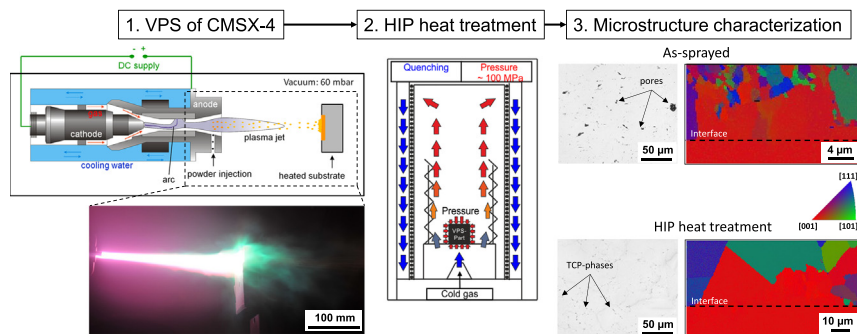
ARTICLE INFO

ABSTRACT

Turbine blades in aviation engines and land based gas-turbines are exposed to extreme environments. They suffer damage accumulation associated with creep, oxidation and fatigue loading. Therefore, advanced repair methods are of special interest for the gas-turbine industry. In this study, CMSX-4 powder is sprayed by Vacuum Plasma Spray (VPS) on single-crystalline substrates with similar compositions. The influence of the substrate temperature is investigated altering the temperature of the heating stage between 850 °C to 1000 °C. Different spray parameters were explored to identify their influence on the microstructure. Hot isostatic pressing (HIP) featuring fast quenching rates was used to minimize porosity and to allow for well-defined heat-treatments of the coatings. The microstructure was analysed by orientation imaging scanning electron microscopy (SEM), using electron backscatter diffraction (EBSD). The effects of different processing parameters were analysed regarding their influence on porosity and grain size. The results show that optimized HIP heat-treatments can lead to dense coatings with optimum γ/γ′ microstructure. The interface between the coating and the substrate is oxide free and shows good mechanical integrity. The formation of fine crystalline regions as a result of fast cooling was observed at the single-crystal surface, which resulted in grain growth during heat-treatment in orientations determined by the crystallography of the substrate.

© 2019 The Authors. Published by Elsevier Ltd. This is an open access article under the CC BY license (http://creativecommons.org/licenses/by/4.0/).

1. Introduction

The hot sections of aircraft engines and stationary gas turbines are exposed to extreme environments, where high temperature creep and

* Corresponding author.
  E-mail address: t.kalfhaus@fz-juelich.de (T. Kalfhaus).

fatigue caused by static and alternating mechanical and thermal stresses drive elementary damage processes which govern the exploitable life of high temperature components. The most critical high temperature components in gas turbines are turbine blades, which are often made of single-crystalline nickel-based superalloys [1,2]. High costs associated with a replacement of single-crystal turbine blades make repair procedures attractive. When new material is added by coating procedures, it is important that the added material is well bonded and has similar mechanical features as the substrate. Ideally, the repaired parts should show similar material properties and performance parameters as the original turbine blades prior to service exposure.

There are four key criteria which lead to a rejection of first stage blades during an engine inspection: The presence of cracks, dimensional discrepancies, local hot corrosion attack and high accumulated creep strains [3]. The hottest section of a turbine blade is its trailing edge, where reactions with the combustion gas promote hot-gas corrosion and oxidation [4].

New repair techniques like laser processing are attractive for the repair of single-crystalline materials [5–10]. They use superalloy powders which are heated and melt/solidify at the substrate surface. The process parameters which control the melt pool can be optimized to enforce epitaxial crystal growth [8]. While preliminary results are promising, certain issues remain to be solved, which are associated with thermal gradients, residual stresses and crack formation [5,7].

Plasma spray processes might also be attractive repair techniques, which yield coatings with well-defined microstructures and desired coating thicknesses. They are widely used e.g. for bond coats [11,12], top coats of thermal barrier coating systems in turbine engines [13,14] and wear protection [15]. Detailed publications on the effect of plasma spray-based repair processes on the microstructures of turbine engine parts are however rare. One detailed study was published by Okazaki et al. [16] who investigated the loss/redistribution of alloy elements associated with high temperature coating of superalloy CMSX-4.

Within the different thermal spray techniques a promising method for the repair of superalloys is especially vacuum plasma spraying (VPS), where a plasma jet is generated by a direct current (DC) plasma torch and the plasma gas usually consists of argon and other secondary gases (hydrogen, nitrogen, helium). The metal powder is injected by a carrier gas (argon) into the plasma, where it immediately melts at temperatures between 8000 and 10,000 K [17]. The droplets are then accelerated towards the substrate surface. A melt pool does not form due to the rapid solidification of the liquid droplets [18]. To lower the oxygen content in the coatings, the process is conducted under controlled Ar atmosphere, at low pressures of about 60 mbar in a vacuum chamber [19]. When the small droplets clash onto the surface, they solidify and form flat material regions which are referred to as splats. Thus a VPS coating is built up from splat layers. The formation of a splat is a complex process which cannot be directly observed. However, it was experimentally shown that higher impact velocities result in lower splat thicknesses [20] and that splat adhesion can be improved with higher substrate temperatures [21]. As material is sprayed onto the substrate, internal interfaces are created, between the substrate and the splats of the first layer, and between the subsequent splat layers. Oxidation can occur at these interfaces and pores can form there [22].

The spatial distribution of particles, often called footprint, impacting on the surface often shows a Gaussian like shape. The bead is formed with a movement of the torch at a relative velocity to the substrate. The bead height (h_b) and width (w) depend on the spray parameters. The overlapping beads form the first spray layer of the coating [17].

Campbell et al. [23] described a VPS repair process for CMSX-4. They used indentation data to retrieve mechanical input data for calculations with the finite element method (FEM), to obtain stress-strain data for the coating material, in the as-sprayed and annealed condition. Their heat-treatment was not sufficient to decrease the porosity. The high quenching rate resulted in an equiaxed grain structure without the formation of detrimental topologically close-packed phases (TCP) at grain

boundaries. The annealing caused a softening of the material. The combined indentation/FEM-method proposed by Campbell [23] has a considerable potential to replace conventional uniaxial testing for materials and coatings.

It has been reported, that the substrate temperature during plasma spraying has a strong influence on the kinetics of the solidification of droplets [21,24–29]. Yoa et al. [24] investigated the epitaxial growth of molten TiO_2 on rutile TiO_2 and on α-Al_2O_3 substrates during APS. They found that this particular growth was significantly influenced by increasing deposition temperatures, and that a minimum temperature of 500 °C was needed to successfully apply the method. Rapid solidification leads to the formation of epitaxial material regions on ⟨100⟩ oriented substrates.

Yang et al. [26] showed that it is possible to promote epitaxial growth on preheated substrates using atmospheric plasma spraying (APS). They used single-crystal α-alumina substrates, preheated to 900 °C and deposited single alumina droplets. Transmission electron microscopy (TEM) investigations showed that the splats exhibited the crystalline structure of the substrates in [001] and [110] orientation. Jiang et al. [25,29] investigated the effects of substrate temperatures on the splat formation of molybdenum and yttrium-stabilized zirconia (YSZ) using plasma spraying. They showed that increased substrate temperatures result in a change of splat morphology from highly fragmented to disc-like.

Higher temperatures lead to a decrease in porosity and result in higher bonding strength between the layers of the coating. Sampath et al. [21] compared splat formation under conditions of VPS and atmospheric plasma spraying. After VPS processing, splats are flatter and more widely spread as compared to APS. Higher particle velocities and the absence of oxidation during VPS result in heterogeneous nucleation of columnar grains with a ⟨100⟩ growth texture within the splats. Crystallographic textures in plasma-sprayed coatings were investigated by Shinoda et al. [27] who used electron-backscatter diffraction (EBSD). They deposited nickel by APS on polished and preheated (500 °C) stainless steel substrates and found a ⟨100⟩ texture, which they explained on the basis of the preferential growth in this direction for cubic materials [21]. Kovarik et al. [30] investigated the influence of substrate temperatures on the properties of APS and VPS tungsten coatings. Their results indicate that changing the substrate temperature results in different splat morphologies, grain sizes and intersplat sintering.

These previous studies suggest that there is an advantage of using VPS over APS, and that one can optimize coating microstructures by increasing substrate temperatures and thus obtain textured coatings which have a good compatibility with the single-crystalline substrate.

Recently, it has been shown [31–34] that heat-treatments using HIP can recover microstructural creep damage and restore initial high temperature strength of crept material states. This rejuvenation heat-treatment as a part of the blade refurbishment procedure eliminates processing and creep porosity from the microstructure. An optimized HIP heat-treatment can also improve the mechanical properties of the coatings by lowering the porosity [35] and optimizing the grain morphology and the γ/γ′ microstructure. In summary, existing information in the literature suggests that VPS repair of single-crystalline substrates in combination with a subsequent HIP heat-treatment merits further attention in single-crystalline turbine blade technology.

Table 1
Nominal compositions in wt% of the alloys used in the present work. The powders were made of the alloy referred to as CMSX-4. The substrate consisted of the alloy referred to as ERBO/1.

Alloy	Composition (wt%)									
	Cr	Co	Mo	Al	Ti	Ta	Hf	W	Re	Ni
CMSX-4 (powder)	6.5	9.8	0.62	5.7	0.97	6.4	0.086	6.4	2.8	bal.
ERBO/1 (substrate)	6.5	9.6	0.6	5.7	1.0	6.5	0.1	6.4	2.9	bal.

Table 2
Size parameters characterizing the particle size distributions for the powder used for spraying (D_x indicate particle size for which x% are below this value).
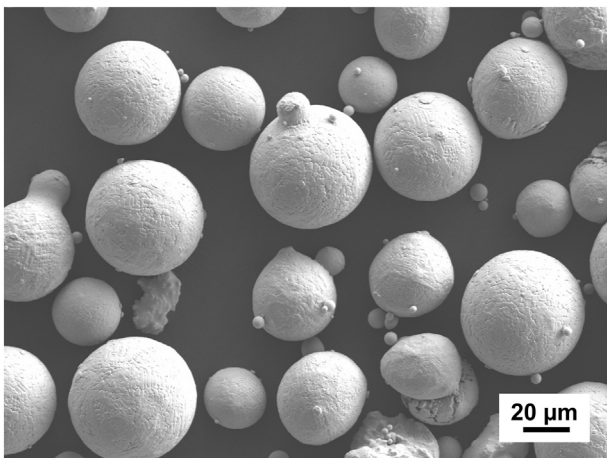
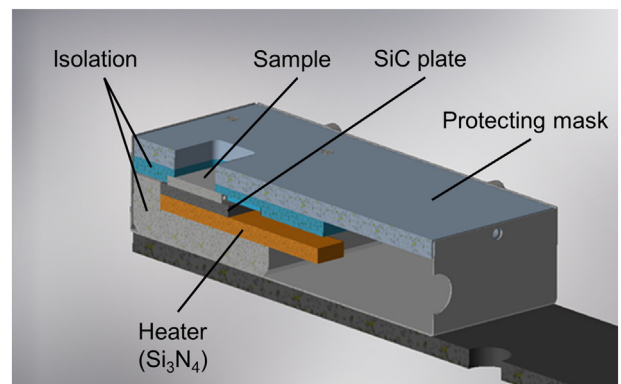| Geom. average	38,5 μm
D_{10}	27,7 μm
D_{50}	39,7 μm
D_{90}	55,5 μm

Table 3
Specimens investigated in the present work together with the corresponding spray parameters.

Sample code	Plasma power (kW)	Powder feeding rate (%)	Stand-off distance (mm)	Scanning speed (mm/s)	Substrate T (°C)	O_2 content [wt%]
A1	47	4	300	100	1000	0,0573
A2	46.9	4	300	250	1000	0,0740
A3	46.8	4	300	500	1000	0,2056
A4	51.1	4	300	500	1000	0,3884
A5	47	4	275	500	1000	0,1031
A6	46.9	4	250	500	1000	0,1309
A7	46.9	8	300	500	1000	0,1114
A8	47	12	300	500	1000	0,0441
B1	46.1	15	275	440	850	–
B2	46.2	15	275	440	900	–
B3	46.4	15	275	440	950	–

In the present study a blade refurbishment procedure including VPS and subsequent HIP heat-treatment is explored. CMSX-4 powder was deposited by VPS on polished single-crystalline ERBO/1 substrate (CMSX-4 type material) [36,37]. The coatings were characterized using laser microscopy, energy-dispersive X-ray spectroscopy (EDS), and orientation imaging scanning electron microscopy (SEM/EBSD). The effects of different processing parameters including the substrate temperature, the plasma power, the spray distance, the scanning speed and the powder feeding rate were investigated with a focus on the resulting microstructures. In addition, a heat-treatment under hydrostatic pressure was performed using HIP. The porosity and grain size of the VP sprayed and HIP heat-treated samples were analysed and compared.

2. Experiments

2.1. Material and specimen production

The substrates and the powder were obtained from a CMSX-4 type alloy. Table 1 shows the compositions of both alloys, that were measured by inductively coupled plasma mass spectrometry (ICP-MS) [34]. Both alloy compositions fall in the compositional range specified for CMSX-4. The ERBO/1 substrates were in a solution annealed state and had a ⟨001⟩ crystal orientation. All details describing the heat-treatment and the microstructure of ERBO/1 have been published elsewhere [31,37,38]. The CMSX-4 powder was produced by gas atomization in Ar atmosphere by TLS Technik GmbH & CO Spezialpulver KG (Bitterfeld-Wolfen; Germany) and vibration sieved to a size of 25–50 μm. The particle size distribution was measured by a laser diffraction particle size analyser LA-950 from HORIBA (Kyoto; Japan) and the results are presented in Table 2. A SEM picture of the powder particles is presented in Fig. 1. The oxygen contents of the powder and samples A1–A8 were measured using a Leco TCH600 (St. Joseph; USA) with a precision of 0.025 ppm. The measured oxygen content of the CMSX-4
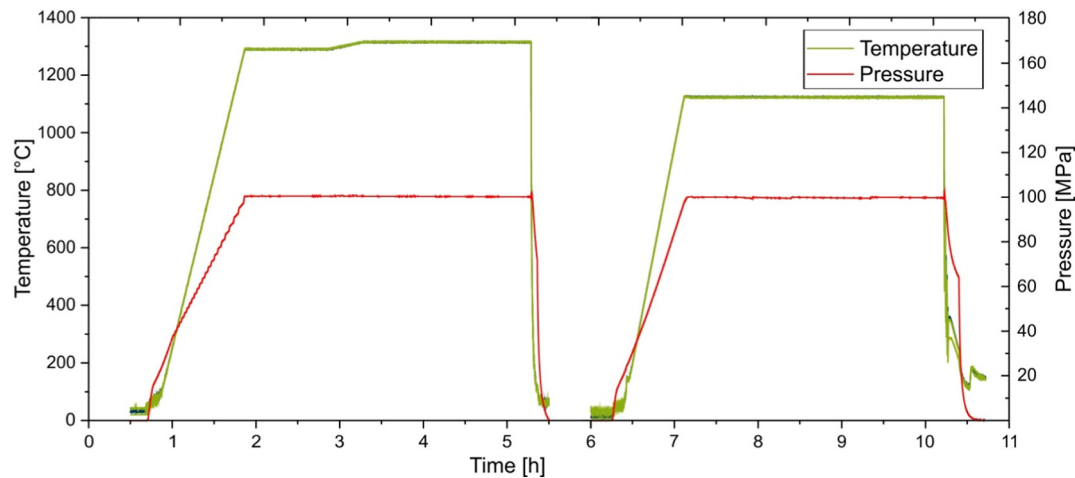
powder was 0.032 wt%. The oxygen content is connected to the appearance of alumina within the coating and the surface of the powder. Sato et al. [39] confirmed that a compact alumina layer forms at temperatures above 1000 °C and proved its stability using an Ellingham diagram. From a thermodynamic point of view, Al_2O_3 already forms at oxygen partial pressures around 10^{-35} atm [40].

The samples were manufactured with an Oerlikon Metco AG (Pfäffikon, Switzerland) Multi Coat VPS-system, using a F4VB spray gun with a 7 mm nozzle diameter. The plasma power of the spray gun, the powder feeding rate, the stand-off distance between the spray gun and the sample and the scanning speed of the spray gun have major influences on the coating formation. Therefore, those parameters were varied to reveal their influence in matters of porosity, grain size and oxygen content of the coatings. This will be discussed in Section 3.2. These relevant spray conditions are summarized in Table 3. The powder was injected radially from the bottom into the plasma jet. The chamber pressure was at 60 mbar argon and the plasma gas consists of 10 normal litres per minute (NLPM) hydrogen and 50 NLPM argon for type A samples and 9 NLPM hydrogen and 50 NLPM argon for type B samples. The hydrogen level for the type A samples was higher to slightly increase the gun power.

The dimensions of the substrates were $32 \times 20 \times 2.5$ mm^3. The substrate contained a 1.1 mm diameter hole which allows us to bring an S-type thermocouple in direct contact with the sample. The samples were cut by electro discharge machining and the surface was ground and polished, in the final step with a 1 μm diamond paste. The resulting surface roughness of Ra ≤0,02 μm was measured with a Cyberscan CT350 from cyber TECHNOLOGIE (Eching; Germany) according to DIN EN ISO 4287. The substrate was heated to the target temperature using a

Fig. 1. SEM-image (secondary electron) of CMSX-4 powder particles taken at an acceleration voltage of 8 kV.

Fig. 2. Heating stage for temperatures up to 1000 °C used during the VPS process.

Fig. 3. Temperature profiles recorded during a two-step HIP treatment. First step: 100 MPa and 1310 °C for 2 h followed by fast quenching. Second step: 100 MPa and 1140 °C for 4 h followed by fast quenching.

1 kW electrical resistance heater from BACH Resistor Ceramics GmbH (Werneuchen; Germany) which was controlled by a Jumo (Fulda; Germany) LR 316 laboratory controller in a desk-top case. The temperature during deposition was logged by an ALMEMO 2690 system manufactured by Ahlborn (Holzkirchen; Germany). Fig. 2 depicts the setup of the heating stage with a customised insulation manufactured by DOTHERM GmbH &Co. KG (Dortmund; Germany) and a SiC plate between the heater and the sample to reduce temperature variations. The housing protects the heater and its connections and the thermocouple. The degree of substrate oxidation during the initial heating was reduced by optimizing the heater control settings and the scanning movement of the plasma plume over the sample surface. The hydrogen content in the plasma provided a reducing atmosphere which also counteracted oxidation.

2.2. Hot isostatic pressing and aging

Hot isostatic pressing was carried out in a HIP unit of type QIH-9 from Quintus Technologies AB (Västeras; Sweden). This HIP unit allows for controlled cooling, and, if needed, ultra-rapid quenching (URQ) [41]. In the present study combined heat-treatments under a hydrostatic pressure were performed.

The solution heat-treatment of the CMSX-4 type single-crystal Ni-base superalloy ERBO/1 was integrated into the HIP treatment in this work. All details regarding the conventional solution heat-treatment and the subsequent aging have been described elsewhere [37]. The HIP-solution-heat-treatment consisted of a 2 hour exposure under an Ar-pressure of 100 MPa at a temperature 1310 °C in a two zone Mo-furnace, followed by ultra-rapid quenching. The first step of the
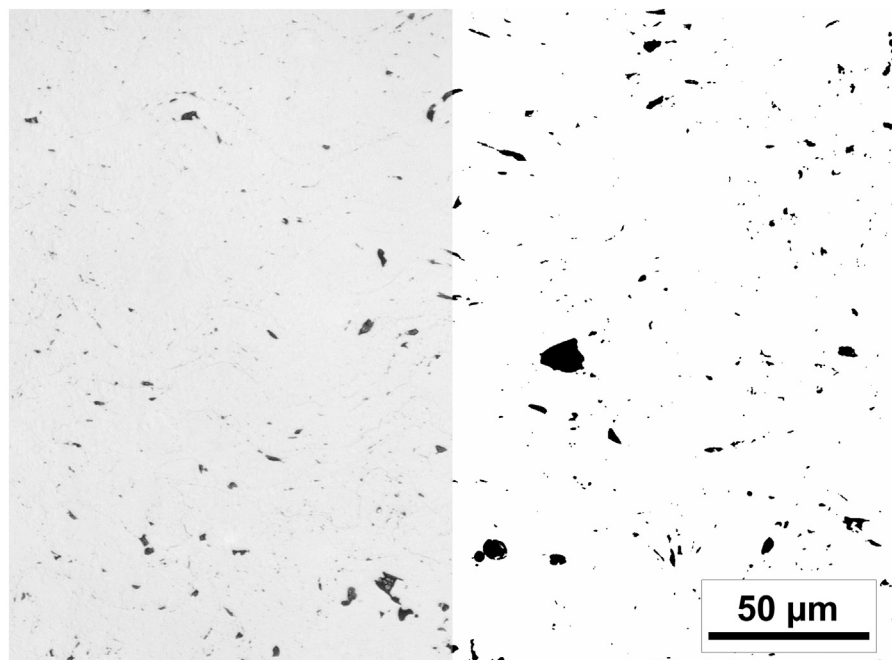
Fig. 4. Using confocal laser microscopy to characterize porosity in sample A7. Left side of image: Experimental image. Right side of image: Experimental image transformed into a binary image for digital image analysis.
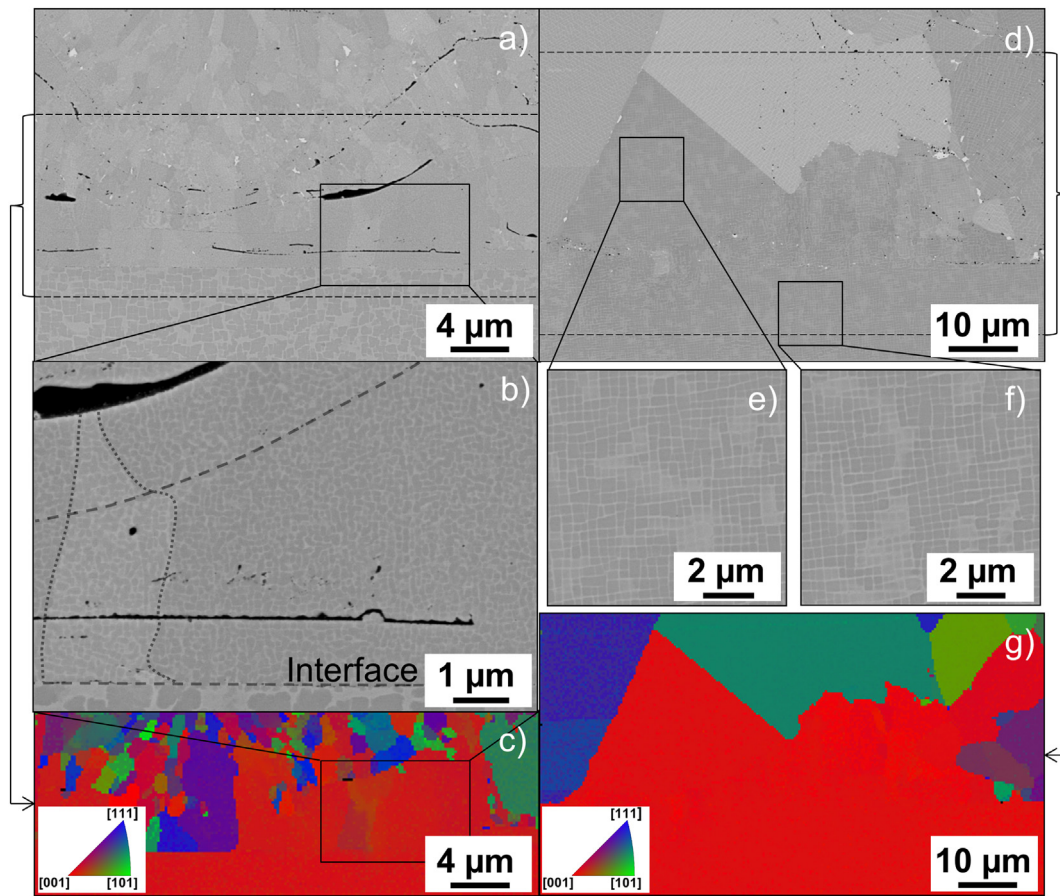
Fig. 5. SEM results from specimens after spraying and after spraying/HIP. SEM performed at an acceleration voltage of 8 kV (BSE). (a) to (c) Specimen A6. (a) Overview SEM micrograph of interface region after spraying. Top: Coating. Bottom: SX substrate. (b) Area highlighted with a black rectangle in panels a and c at higher magnification. The lower dashed line shows the substrate/coating interface. The upper dashed line indicates a splat/splat interface. Dotted line shows a grain with a slight misorientation. (c) Colour coded EBSD information on the region between the two horizontal dashed lines in panel a. (d) to (g) Specimen A6 after heat-treatment (d) SEM micrograph taken after spraying and HIPing. Two regions are highlighted by black squares. (e) and (f) Regions highlighted in panel d at higher magnification. (g) Colour coded EBSD information from the region between the two dashed lines in panel d. (For interpretation of the references to colour in this figure legend, the reader is referred to the web version of this article.)

subsequent precipitation heat-treatment (aging) was performed at 1140 °C for 4 h and an Ar-pressure of 100 MPa. The temperature and pressure profiles recorded during the experiments are shown in Fig. 3. The second precipitation heat-treatment (aging) step at 870 °C for 16 h, was carried out with all samples in a furnace under Ar-atmosphere.

2.3. Microstructural examination

The porosity of all samples was characterized using a confocal laser microscope Keyence (Osaka; Japan) VK-9710 with a wavelength of 408 nm in combination with quantitative image analysis. For each sample, seven micrographs were taken at a 50× magnification. The
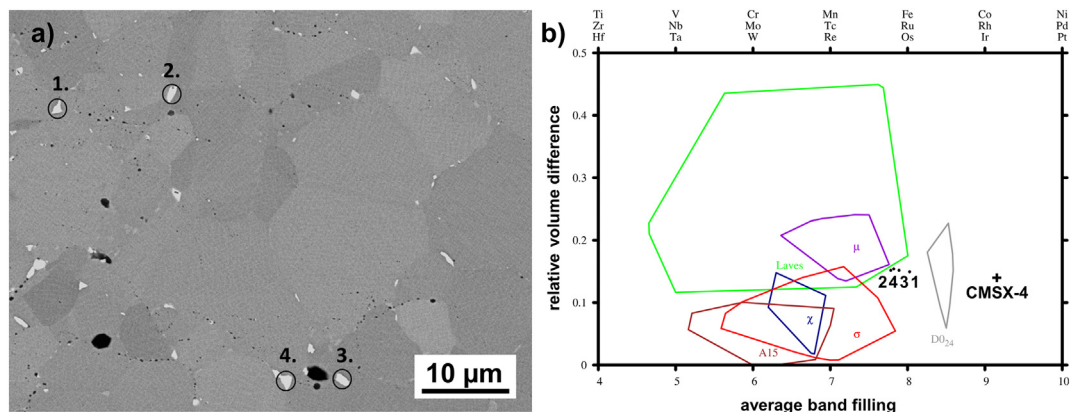
Fig. 6. TCP phase information on four precipitates from the HIPed sample A3. (a) Position of four precipitates in a SEM micrograph (BSE). (b) Composition of CMSX-4 (average composition: +-sign on the right) and of the four precipitates in the structure map.

Table 4
EDS results for the four TCP phase precipitations shown in Fig. 6 (Specimen: A3).

Position	Composition (at.%)						
	Al	Cr	Co	Ni	Mo	W	Re
1	0.5	19.4	20	25.1	2.3	12.5	20.2
2	0.8	22	19.1	24.7	2.5	11.5	19.3
3	1.3	18.3	19.1	30.9	1.8	10.8	17.8
4	1.3	20.5	18.7	27.6	2.2	11.2	18.5

micrographs were analysed with Analysis Pro. The pixel size limits the detectable pore diameter to about 0.2 μm. Fig. 4 shows the original micrograph of specimen A7 from Table 2 together with the associated digital binary image, which was evaluated by the image analysis software. SEM imaging and EDX/EBSD investigations were carried out on a Zeiss Ultra 55 FEG-SEM (Oberkochem; Germany) equipped with an EDX INCA and Crystal Analysis System from Oxford Instruments. Electron backscatter diffraction measurements (EBSD) to analyse grain sizes were performed on a scanning electron microscope (SEM) of type Quanta FEI 650 ESEM (Hillsboro; USA) equipped with a Hikari XP camera (EDAX, AMETEK). These measurements were performed using an accelerating voltage of either 15 kV or 30 kV, a working distance of 15 mm - 19 mm and step sizes between 0.1 μm and 0.75 μm. Magnifications between 400 and 2000 were applied, which results in inverse pole figure (IPF) coloured maps with a resolution of 2048 × 1536 pixels. Kikuchi patterns were indexed using the software TSL OIM (v. 6.2.0). Grain sizes are expressed in terms of the equivalent circle diameter (ECD), which was calculated from the measured areas of the grains in the metallographic cross-section.

3. Results and discussion

3.1. Microstructural features of interfaces

All SEM micrographs taken from interface regions in the as-sprayed conditions for all type A samples (Table 3) look similar. As an example, the SEM micrograph of sample A6 is shown in Fig. 5a. The polished single-crystalline substrate contains irregular γ′ precipitates. A few single splats are visible in the dense coating, which show intersplat porosity and thin oxide scales. Fig. 5b shows the interface at a higher magnification. A very fine dispersion of complex shaped γ′ particles can now be recognized, which forms as a result of the slow cooling of the sample after powder deposition in the VPS chamber.

The dashed lines at the bottom of the picture indicate the position of the interface between the substrate and the coating. Above this interface in a distance of 1 μm, one can recognize a thin intersplat pore. The first splat that hit the substrate has a thickness of 1 μm. It is well bonded and shows no obvious oxygen contamination. The dashed line in the upper part of the picture indicates the position of an interface between two splats. The dashed lines in Fig. 5a highlight the regions from

where the EBSD map in Fig. 5c was obtained. The elongated grains on the left side of Fig. 5c indicate columnar grain growth. Fig. 5b shows a grain with a slight misorientation (marked by a dotted line). The grain grew through the intersplat pore and the interface of the two splats. The red colour of the substrate confirms the [001]-orientation of the single-crystalline substrate and the epitaxial growth in sections of the coating on the polished substrate (see colour coding in the IPF inset). Since the height of this area is about 5 μm, several splats continued to solidify in the [001] direction.

The recrystallization of the coating during the HIP heat-treatment leads to grain growth and an equiaxed grain structure, Fig. 5d. During the HIP treatment, the porosity decreases and fine oxide scales mark the original splat microstructure. It is difficult to see the original splat interfaces. These can only be recognized on the right side of the image, because they are marked by fine oxides. The EBSD results indicate the crystal orientation and reveal a [001] direction of the grain with a triangular shape and a maximum height of about 30 μm. It is assumed that this grain grew from an area that nucleated at the substrate. Straight grain boundaries indicate an energy minimum since the driving force for grain growth in the absence of dislocations is only dependent on the radius of the grain boundary [42]. Fig. 5e and f shows a coating/substrate detail at a higher magnification. Both areas show the same γ′ volume fractions of about 75%, and in both cases the ordered cuboidal γ′ particles have an average edge length of 0,5 μm while the γ channels have an average width of 100 nm [31]. An epitaxially grown coating on a single-crystalline super alloy substrate, is expected to show good adhesive strength.

Previous work on as-cast ERBO/1 [43] showed the formation of TCP phases of μ, Laves and σ type in interdendritic regions. This is related to the evolution of the local chemical composition during solidification [44]. The σ phase precipitates dissolve during the HIP treatments of cast ERBO/1 [43] after 32 h at 1000 °C, while the μ and Laves phase precipitates withstand 1200 °C over time periods of 8 h. As-sprayed CMSX-4 also shows TCP phase precipitates, predominantly at grain boundaries (see Figs. 5a and 3a in Campbell et al. [23]). These completely dissolve after 6 h at 1315 °C and do not re-precipitate during ice water quenching (Fig. 3b in Campbell et al. [23]), similar to the complete dissolution in cast ERBO/1 after 8 h at 1200 °C reported in [43]. This indicates that the TCP phases dissolve during the solution annealing step and form during the first and second aging step of the heat-treatment as shown in Fig. 6a.

A closer look was taken at the TCP phase precipitates. In particular, the local chemical compositions obtained by EDX (Table 4) are compared with the thermodynamic stability of TCP phases in bulk materials of the same chemical composition, which are predicted using a structure map [45]. The structure map has been successfully applied to the identification of TCP phase precipitates as has been previously described [43,44]. The present structure-map analysis is shown in Fig. 6b. The cross marks the composition of CMSX-4 in the structure map. We find that the experimentally determined chemical composition of the TCP
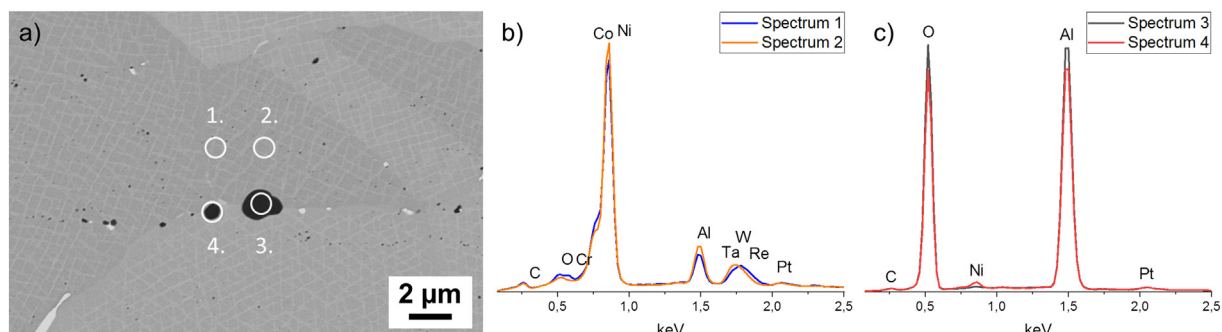
Fig. 7. SEM results obtained at an acceleration voltage of 8 kV. (a) SEM micrograph (BSE) where two alloy locations (1 and 2) and two oxides (3 and 4) are highlighted by white circles. (b) and (c) Corresponding EDS spectra calculated based on 45,068 counts.
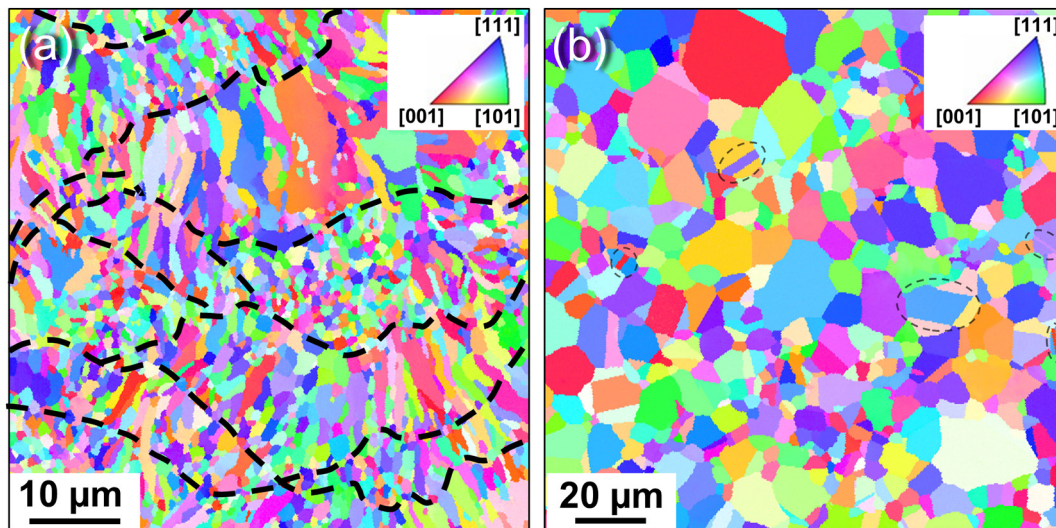
Fig. 8. Colour coded EBSD maps illustrating the effect of a post-spray HIP treatment. The colour coding is defined in the IPD maps in the upper right of the images. (a) As-sprayed coating. Dashed lines help to appreciate the splat structure. (b) After spraying and HIP treatment. Twins are highlighted with dashed lines. (For interpretation of the references to colour in this figure legend, the reader is referred to the web version of this article.)

phase precipitates in our samples are close to the regions of stability of the μ and Laves bulk phases in the structure map. Due to the small size of the precipitates, the measured chemical compositions may include contributions from the matrix that would lead to a shift towards the nominal chemical composition of CMSX-4. Therefore, the experimental results are considered to be in line with the structure map analysis. A TEM investigation of CMSX-4 produced by selective electron beam melting revealed the presence of μ phase type precipitations on high angle grain boundaries [46]. These results suggest that μ phase precipitates are expected to form in sprayed CMSX-4 during HIP heat-treatments.

To decrease the size of the interaction volume which emits X-rays stimulated by electron bombarded during EDS analysis, the acceleration voltage was lowered to 8 kV. Such measurements were performed for the four positions highlighted by white circles in Fig. 7a. The EDS results in Fig. 7b and c show for spectrum 3 and 4 high oxygen and aluminium peaks. They confirm the presence of alumina in the coating, which results from a slight oxidation of the substrate surface or of the powder, either due to a contamination of argon with oxygen or to a leakage of the vacuum chamber vessel. The residual presence of oxygen is unavoidable.

In Fig. 8 representative results from EBSD measurements are given. Fig. 8a shows the microstructure in the as-sprayed condition of sample B2. The dashed lines indicate the original positions of single splats which form as the coating is built-up by VPS. Sampath et al. [21] observed a similar texture of nickel deposits with a columnar microstructure in the core region of the splat. Even though the individual splat might be textured, with many individual splats solidifying, the coating microstructure develops no significant texture. After a HIP treatment the microstructure changed, Fig. 8b. Grain growth is observed after HIP treatment. Additionally, larger grains with coherent twins (twin boundaries: $\Sigma = 3$) appear in the microstructure, which represents direct experimental evidence for recrystallization.

3.2. Influence of spray parameters on microstructure
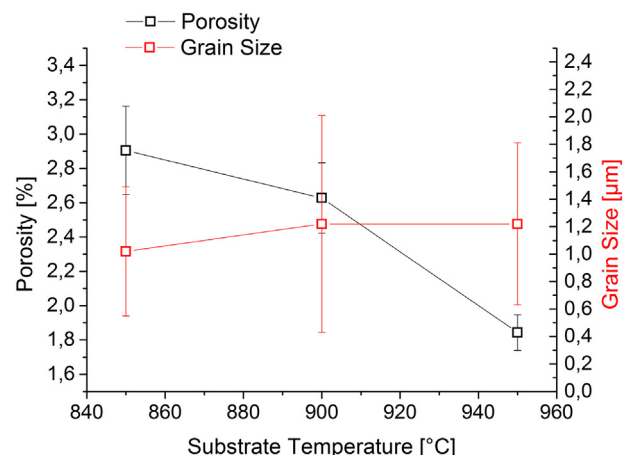
3.2.1. Porosity

The porosity is influenced by numerous spray parameters during VPS coating. Figs. 9 and 10 show the influence of the substrate temperature, the stand-off distance, the scanning speed, the powder feeding rate and the power of the spray gun. The main reason for an increase in porosity is the evolving splat structure, the solidification speed and

the dimension of the bead. The influence of the substrate temperature is shown in Fig. 9. The porosity decreases with increasing substrate temperatures, since the splats show more pronounced flattening on the substrate. Smaller pores arise when solidification is slower, since the time the material has a low viscosity is longer and porous regions can be filled with material.

The influence of the remaining parameters is presented in Fig. 10. The stand-off distance affects the dimensions of the bead and the particle temperature and velocity, Fig. 10a. The bead is in focus at rather small stand-off distances with increased local temperatures and expands with larger distances. Low velocities and lower temperatures of the particles with an increasing stand-off distance result in more viscous particles, faster solidification, a change in the splat morphology and larger pores.

The scanning speed influences the thickness of the bead. More particles per area impact the substrate surface at slower scanning speeds. Local temperatures of the substrate increase since a smaller area is exposed to the same plasma power. As discussed above slow solidification and a reduced viscosity result in less intersplat porosity, Fig. 10b.

The powder feeding rate has a similar influence on the bead. Higher powder feeding rates result in more energy consumption of the plasma power, since more mass per time is heated. Hence the powder temperature decreases, the splat flattening is reduced and the porosity

Fig. 9. Influence of substrate temperature on porosity and grain size. Samples: B1–B3.
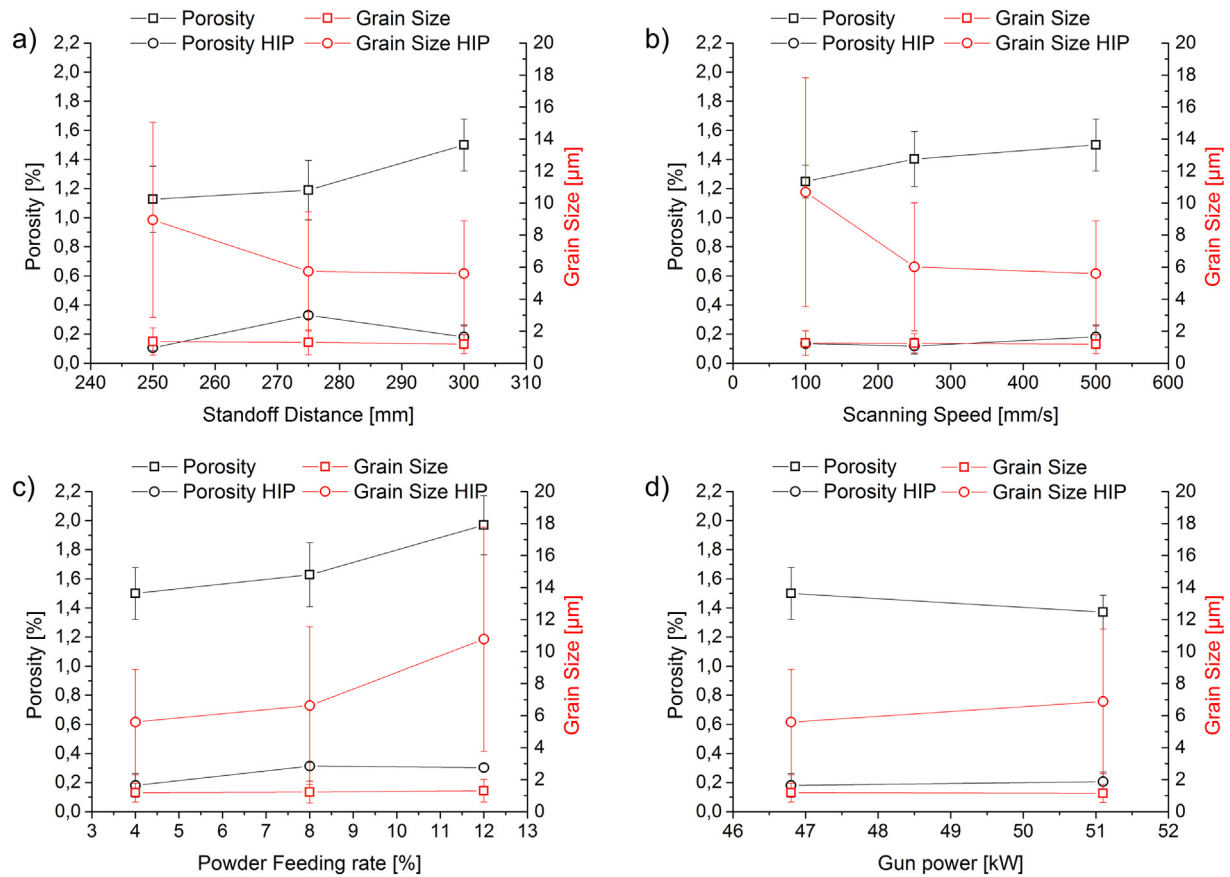
Fig. 10. Influence of processing parameters on porosity and grain size of as-sprayed and sprayed/HIPed samples A1 to A8. (a) Stand-off distance. (b) Scanning speed. (c) Powder feeding rate. (d) Gun power.
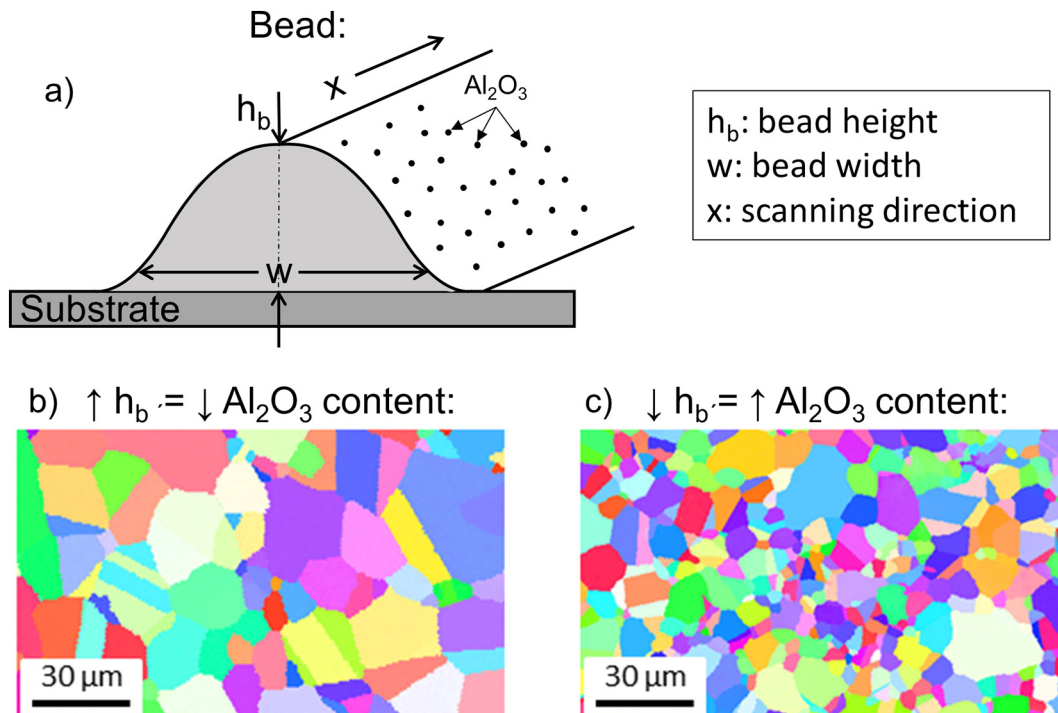
Fig. 11. Influence of bead height and Al_2O_3 content on grain size. (a) Schematic illustration of bead together with arriving Al_2O_3 particles. (b) Colour coded EBSD map showing large grains for a large bead height (sample A8). (c) Colour coded EBSD map of sample A3, where grain sizes are small due to smaller bead heights. For details see text. (For interpretation of the references to colour in this figure legend, the reader is referred to the web version of this article.)

increases, Fig. 10c. Local temperatures increase with higher powder feeding rates.

As a result of an increased gun power, the particle temperatures increase with a reduced viscosity, the solidification rate decreases, resulting in smaller pores. As stated earlier under these conditions the forming splat can more easily adapt to the substrate/coating profile and the topography of the previous splat can be accommodated more accurately leading to lower porosity levels, Fig. 10d.

Fig. 10 also shows results which were obtained after HIP treatments. The high pressures during the heat-treatment lead to the closure of the pores within the coating and a residual average porosity of only 0.21 ± 0.09 area %. This corresponds to an average porosity reduction of the samples by 1.22 ± 0.24 area %. The porosity level of the HIPed coating is therefore lower than the corresponding porosity level of as-cast ERBO-1 (0.3%) [31].

A regression analysis for the as-sprayed porosity values shows a similar significance for all processing parameters. The linear fit and a standardisation of variables show the same influence of each spray parameter on the porosity.

3.2.2. Grain size

The variation of different parameters has a minor influence on the grain size of the samples in the as-sprayed condition, Fig. 10. The substrate temperature has the strongest influence on the solidification speed of the molten droplets, Fig. 9. Rapid cooling and fast solidification of the splats result in small grain sizes for a substrate temperature of 850 °C. An increase of the substrate temperature leads to a minor increase of the grain size.

The average grain size for the as-sprayed coatings is 1.3 ± 0.1 μm, Figs. 9 and 10. The HIP heat-treatment results in recrystallization and growth of the grains to sizes larger than 5 μm. Smaller stand-off distances, slower scanning speeds and higher powder feeding rates result in larger grains after the heat-treatment, Fig. 10. As discussed in the following, it is believed that the oxygen content (Al_2O_3) influences the grain growth. Parameter settings that lead to large grains result in an increase of the bead height (h_b) and faster coating formation. Fig. 11a illustrates the formation of the bead with a formation of Al_2O_3 on the hot surface. Thicker beads expose a smaller surface area to the atmosphere. Small aluminium oxide particles form even at low oxygen partial pressures. They can enter the coating material and have the potential to pin grain boundaries and thus slow down grain growth. The oxygen contents of samples A1, A6 and A8 (Table 3) are reduced in comparison to the standard sample A3 with a smaller h_b. The EBSD maps in Fig. 11c show that the thin layers of sample A3 with a higher oxide content in comparison to sample A8 (Fig. 11b) reveal smaller grains after the heat-treatment. This explains the evolution of the large grain sizes with rather low scanning speeds, small stand-off distances and high powder feeding rates. Fig. 10 shows that an increase in gun power decreases the grain size after the heat-treatment. Sample A4 (Table 3) shows the highest oxygen content of all samples due to an increased particle temperature and therefore faster oxidation.

The combination of high substrate temperatures, small stand-off distances, slow scanning speeds and low powder feeding rates should result in an increase of the grain sizes after the HIP treatment. Materials with large grains show better creep properties since the grain boundaries represent weak links in the microstructure. The porosity associated with spraying can be removed by a HIP heat-treatment. An analysis of the results obtained in the present work shows that all spray/processing parameters can affect the microstructure. However, the powder feeding rate and the spray distance have the strongest influence on the grain size which evolves during HIP exposure.

4. Summary and conclusions

In the present work the potential of vacuum plasma spraying (VPS) as a possible repair technique for single crystalline nickel-based superalloys is assessed, with a special focus on the substrate/coating microstructures. From the results obtained in the present work, the following conclusions can be drawn:

- It is beneficial to apply VPS repair coating layers to single-crystalline nickel-based superalloy substrates at high substrate temperatures of the order of 1000 °C.
- The evolution of microstructures in the substrate/coating regions starts with the formation of splats (small crystalline material volumes which form on the substrate surface by VPS deposition followed by fast solidification). A subsequent HIP treatment results in epitaxial grain growth in sections of the coating. The superalloy heat-treatment can be integrated into the HIP procedure.
- The influence of different spray parameters such as substrate temperature, stand-off distance, scanning speed, gun power and powder feeding rates were investigated. All parameters have a direct influence on the bead properties and the splat formation, and thus govern the evolution of the microstructure during vacuum plasma spray coating.
- As a result of a HIP heat-treatment, grains grow and pores shrink. A set of optimum processing parameters which suppresses porosity and promotes grain growth is thus expected to improve creep properties.
- HIP heat-treatments similarly affect the dissolution of TCP phase precipitates in sprayed and as-cast Ni-base superalloys.
- In summary, the combination of repair coatings produced by VPS and an additional HIP heat-treatment is a promising refurbishment technique for single crystalline blades that show structural damages where material is lost due to oxidation, erosion or dimensional discrepancies after creep damage.

CRediT authorship contribution statement

T. Kalfhaus: Conceptualization, Investigation, Data curation, Project administration, Visualization, Writing - original draft. **M. Schneider:** Investigation, Visualization, Writing - original draft. **B. Ruttert:** Visualization, Writing - original draft. **D. Sebold:** Visualization, Investigation, Validation. **T. Hammerschmidt:** Software, Validation, Writing - original draft. **J. Frenzel:** Visualization, Methodology, Writing - review & editing. **R. Drautz:** Supervision, Funding acquisition, Writing - review & editing. **W. Theisen:** Supervision, Funding acquisition, Writing - review & editing. **G. Eggeler:** Supervision, Funding acquisition, Resources, Writing - review & editing. **O. Guillon:** Supervision, Resources, Writing - review & editing. **R. Vassen:** Supervision, Formal analysis, Resources, Funding acquisition, Writing - review & editing.

Acknowledgment

References

[1] D. Goldschmidt, Einkristalline Gasturbinenschaufeln aus Nickelbasis-Legierungen. Teil I: Herstellung und Mikrogefüge, Mater. Werkst. 25 (1994) 311–320, https://doi.org/10.1002/mawe.19940250804.

[2] R.C. Reed, The Superalloys, Cambridge University Press, Cambridge, 2006https://doi.org/10.1017/CBO9780511541285.

[3] K.C. Antony, G.W. Goward, Aircraft gas turbine blade and vane repair, Superalloys 1988 (Sixth Int. Symp., TMS) 1988, pp. 745–754, https://doi.org/10.7449/1988/Superalloys_1988_745_754.

[4] J.-C. Han, S. Dutta, S. Ekkad, Gas Turbine Heat Transfer and Cooling Technology, second edition CRS Press, 2012.

[5] B. Rottwinkel, C. Nölke, S. Kaierle, V. Wesling, Crack repair of single crystal turbine blades using laser cladding technology, Procedia CIRP 22 (2014) 263–267, https://doi.org/10.1016/j.procir.2014.06.151.

[6] S. Kaierle, L. Overmeyer, I. Alfred, B. Rottwinkel, J. Hermsdorf, V. Wesling, N. Weidlich, Single-crystal turbine blade tip repair by laser cladding and remelting,

CIRP J. Manuf. Sci. Technol. 19 (2017) 196–199, https://doi.org/10.1016/j.cirpj.2017.04.001.

[7] B. Rottwinkel, L. Schweitzer, C. Noelke, S. Kaierle, Challenges for single-crystal (SX) crack cladding, Phys. Procedia 56 (2014) 301–308, https://doi.org/10.1016/j.phpro.2014.08.175.

[8] M. Gäumann, C. Bezençon, P. Canalis, W. Kurz, Single-crystal laser deposition of superalloys: processing-microstructure maps, Acta Mater. 49 (2001) 1051–1062, https://doi.org/10.1016/S1359-6454(00)00367-0.

[9] R. Vilar, A. Almeida, Repair and manufacturing of single crystal Ni-based superalloys components by laser powder deposition—a review, J. Laser Appl. 27 (2015)https://doi.org/10.2351/1.4862697 (17004-15001).

[10] Z. Liu, H. Qi, L. Jiang, Control of crystal orientation and continuous growth through inclination of coaxial nozzle in laser powder deposition of single-crystal superalloy, J. Mater. Process. Technol. 230 (2016) 177–186, https://doi.org/10.1016/j.jmatprotec.2015.11.017.

[11] M. Subanovic, P. Song, E. Wessel, R. Vassen, D. Naumenko, L. Singheiser, W.J. Quadakkers, Effect of exposure conditions on the oxidation of MCrAlY-bondcoats and lifetime of thermal barrier coatings, Surf. Coat. Technol. 204 (2009) 820–823, https://doi.org/10.1016/j.surfcoat.2009.09.056.

[12] P. Song, D. Naumenko, R. Vassen, L. Singheiser, W.J. Quadakkers, Effect of oxygen content in NiCoCrAlY bondcoat on the lifetimes of EB-PVD and APS thermal barrier coatings, Surf. Coat. Technol. 221 (2013) 207–213, https://doi.org/10.1016/j.surfcoat.2013.01.054.

[13] D. Stöver, G. Pracht, H. Lehmann, M. Dietrich, J.-E. Döring, R. Vaßen, New material concepts for the next generation of plasma-sprayed thermal barrier coatings, J. Therm. Spray Technol. 13 (2004) 76–83, https://doi.org/10.1361/10599630418176.

[14] H.B. Guo, R. Vaßen, D. Stöver, Atmospheric plasma sprayed thick thermal barrier coatings with high segmentation crack density, Surf. Coat. Technol. 186 (2004) 353–363, https://doi.org/10.1016/j.surfcoat.2004.01.002.

[15] M. Bitzer, N. Rauhut, G. Mauer, M. Bram, R. Vaßen, H.-P. Buchkremer, D. Stöver, M. Pohl, Cavitation-resistant NiTi coatings produced by low-pressure plasma spraying (LPPS), Wear. 328–329 (2015) 369–377, https://doi.org/10.1016/j.wear.2015.03.003.

[16] M. Okazaki, I. Ohtera, Y. Harada, Damage repair in CMSX-4 alloy without fatigue life reduction penalty, Metall. Mater. Trans. A 35 (2004) 535–542, https://doi.org/10.1007/s11661-004-0364-5.

[17] P.L. Fauchais, J.V.R. Heberlein, M.I. Boulos, Thermal Spray Fundamentals, Springer Sci. Media, 2014 450, https://doi.org/10.1007/978-0-387-68991-3.

[18] R.B. Heimann, Particle-substrate interactions, Plasma-spray Coat. - Princ. Appl, John Wiley & Sons 1996, pp. 137–149.

[19] G. Mauer, R. Vaßen, D. Stöver, Controlling the Oxygen Contents in Vacuum Plasma Sprayed Metal Alloy Coatings, 2006https://doi.org/10.1016/j.surfcoat.2006.10.008.

[20] M. Mutter, G. Mauer, R. Mücke, O. Guillon, R. Vaßen, Correlation of splat morphologies with porosity and residual stress in plasma-sprayed YSZ coatings, Surf. Coat. Technol. 318 (2017) 157–169, https://doi.org/10.1016/j.surfcoat.2016.12.061.

[21] S. Sampath, H. Herman, Rapid solidification and microstructure development during plasma spray deposition, J. Therm. Spray Technol. 5 (1996) 445–456, https://doi.org/10.1007/BF02645275.

[22] E.J. Lavernia, Y. Wu, J.W. & S. Ltd, Heat transfer and solidification of droplets, Spray At. Depos, John Wiley 1996, pp. 331–342.

[23] J.E. Campbell, T. Kalfhaus, R. Vassen, R.P. Thompson, J. Dean, T.W. Clyne, Mechanical properties of sprayed overlayers on superalloy substrates, obtained via indentation testing, Acta Mater. 154 (2018) 237–245, https://doi.org/10.1016/J.ACTAMAT.2018.05.043.

[24] S.-W. Yao, T. Liu, C.-J. Li, G.-J. Yang, C.-X. Li, Epitaxial growth during the rapid solidification of plasma-sprayed molten TiO2 splat, Acta Mater. 134 (2017) 66–80, https://doi.org/10.1016/j.actamat.2017.05.052.

[25] S. Sampath, X. Jiang, J. Matejicek, A. Leger, A. Vardelle, Substrate temperature effects on splat formation, microstructure development and properties of plasma sprayed coatings part I: case study for partially stabilized zirconia, Mater. Sci. Eng. A 272 (1999) 181–188, https://doi.org/10.1016/S0921-5093(99)00459-1.

[26] E.J. Yang, G.J. Yang, X.T. Luo, C.J. Li, M. Takahashi, Epitaxial grain growth during splat cooling of alumina droplets produced by atmospheric plasma spraying, J. Therm. Spray Technol. (2013) 152–157, https://doi.org/10.1007/s11666-012-9862-y.

[27] K. Shinoda, M. Demura, H. Murakami, S. Kuroda, S. Sampath, Characterization of crystallographic texture in plasma-sprayed splats by electron-backscattered diffraction, Surf. Coat. Technol. 204 (2010) 3614–3618, https://doi.org/10.1016/j.surfcoat.2010.04.023.

[28] S. Sampath, X. Jiang, Splat formation and microstructure development during plasma spraying: deposition temperature effects, Mater. Sci. Eng. A 304–306 (2001) 144–150, https://doi.org/10.1016/S0921-5093(00)01464-7.

[29] X. Jiang, J. Matejicek, S. Sampath, Substrate temperature effects on the splat formation, microstructure development and properties of plasma sprayed coatings, Mater. Sci. Eng. A 272 (1999) 189–198, https://doi.org/10.1016/S0921-5093(99)00461-X.

[30] O. Kovářík, P. Haušild, J. Siegl, T. Chráska, J. Matějíček, Z. Pala, M. Boulos, The influence of substrate temperature on properties of APS and VPS W coatings, Surf. Coat. Technol. 268 (2015) 7–14, https://doi.org/10.1016/J.SURFCOAT.2014.07.041.

[31] B. Ruttert, D. Bürger, L.M. Roncery, A.B. Parsa, P. Wollgramm, G. Eggeler, W. Theisen, Rejuvenation of creep resistance of a Ni-base single-crystal superalloy by hot isostatic pressing, Mater. Des. 134 (2017) 418–425, https://doi.org/10.1016/j.matdes.2017.08.059.

[32] L. Mujica Roncery, I. Lopez-Galilea, B. Ruttert, D. Bürger, P. Wollgramm, G. Eggeler, W. Theisen, On the effect of hot isostatic pressing on the creep life of a single crystal superalloys, Adv. Eng. Mater. 18 (2016) 1381–1387, https://doi.org/10.1002/adem.201600071.

[33] B. Ruttert, O. Horst, I. Lopez-galilea, D. Langenkämper, A. Kostka, C. Somsen, J.V. Goerler, M.A. Ali, O. Shchyglo, I. Steinbach, G. Eggeler, W. Theisen, Rejuvenation of single-crystal Ni-base superalloy turbine blades: unlimited service life? Metall. Mater. Trans. A. (2018) 1–12, https://doi.org/10.1007/s11661-018-4745-6.

[34] B. Ruttert, M. Ramsperger, L. Mujica Roncery, I. Lopez-Galilea, C. Körner, W. Theisen, Impact of hot isostatic pressing on microstructures of CMSX-4 Ni-base superalloy fabricated by selective electron beam melting, Mater. Des. 110 (2016) 720–727, https://doi.org/10.1016/J.MATDES.2016.08.041.

[35] K.A. Khor, N.L. Loh, Hot isostatic pressing of plasma sprayed thermal barrier coating systems, Mater. Manuf. Process. 10 (1995) 1241–1256, https://doi.org/10.1080/10426919508935105.

[36] V. Yardley, I. Povstugar, P.-P. Choi, D. Raabe, A.B. Parsa, A. Kostka, C. Somsen, A. Dlouhy, K. Neuking, E.P. George, G. Eggeler, On local phase equilibria and the appearance of nanoparticles in the microstructure of single-crystal Ni-base superalloys, Adv. Eng. Mater. 18 (2016) 1556–1567, https://doi.org/10.1002/adem.201600237.

[37] A.B. Parsa, P. Wollgramm, H. Buck, C. Somsen, A. Kostka, I. Povstugar, P.-P. Choi, D. Raabe, A. Dlouhy, J. Müller, E. Spiecker, K. Demtroder, J. Schreuer, K. Neuking, G. Eggeler, Advanced scale bridging microstructure analysis of single crystal Ni-base superalloys, Adv. Eng. Mater. 17 (2015) 216–230, https://doi.org/10.1002/adem.201400136.

[38] M.S.A. Karunaratne, C.M.F. Rae, R.C. Reed, On the microstructural instability of an experimental nickel-based single-crystal superalloy, Metall. Mater. Trans. A. 32 (2001) 2409–2421, https://doi.org/10.1007/s11661-001-0032-y.

[39] A. Sato, Y.-L. Chiu, R.C. Reed, Oxidation of nickel-based single-crystal superalloys for industrial gas turbine applications, Acta Mater. 59 (2011) 225–240, https://doi.org/10.1016/j.actamat.2010.09.027.

[40] Per Kofstad, Fundamentals of high temperature oxidation/corrosion, High Temp. Corros, Elsevier Applied Science 1988, p. 5.

[41] L. Mujica Roncery, I. Lopez-Galilea, B. Ruttert, S. Huth, W. Theisen, Influence of temperature, pressure, and cooling rate during hot isostatic pressing on the microstructure of an SX Ni-base superalloy, Mater. Des. 97 (2016) 544–552, https://doi.org/10.1016/J.MATDES.2016.02.051.

[42] Gottstein, Kornvergrößerung, Phys. Grundlagen Der Mater, Springer-Verlag 2007, pp. 343–348.

[43] I. Lopez-Galilea, J. Koßmann, A. Kostka, R. Drautz, L. Mujica Roncery, T. Hammerschmidt, S. Huth, W. Theisen, The thermal stability of topologically close-packed phases in the single-crystal Ni-base superalloy ERBO/1, J. Mater. Sci. 51 (2016) 2653–2664, https://doi.org/10.1007/s10853-015-9579-7.

[44] J. Koßmann, C.H. Zenk, I. Lopez-Galilea, S. Neumeier, A. Kostka, S. Huth, W. Theisen, M. Göken, R. Drautz, T. Hammerschmidt, Microsegregation and precipitates of an as-cast Co-based superalloy—microstructural characterization and phase stability modelling, J. Mater. Sci. 50 (2015) 6329–6338, https://doi.org/10.1007/s10853-015-9177-8.

[45] B. Seiser, R. Drautz, D.G. Pettifor, TCP phase predictions in Ni-based superalloys: structure maps revisited, Acta Mater. 59 (2011) 749–763, https://doi.org/10.1016/J.ACTAMAT.2010.10.013.

[46] A. Parsa, M. Ramsperger, A. Kostka, C. Somsen, C. Körner, G. Eggeler, A.B. Parsa, M. Ramsperger, A. Kostka, C. Somsen, C. Körner, G. Eggeler, Transmission electron microscopy of a CMSX-4 Ni-base superalloy produced by selective electron beam melting, Metals 6 (2016) 258, https://doi.org/10.3390/met6110258.